Deep fault-controlled fluid flow driving shallow stratigraphically-constrained gas hydrate formation: Urutī Basin, Hikurangi Margin, New Zealand

Andrew R. Gorman[1], Gareth J. Crutchley[2], Dylan R. Baker[1], Douglas R.A. Fraser[1], Stuart A. Henrys[3], Anne M. Tréhu[4], Robert N. Harris[4], Benjamin J. Phrampus[4,5], Ingo A. Pecher[6,7]

[1]Department of Geology, University of Otago, PO Box 56, Dunedin 9054, New Zealand

[2]GEOMAR Helmholtz Zentrum für Ozeanforschung Kiel, Wischhofstr. 1-3, 24148 Kiel, Germany

[3]GNS Science, PO Box 30368, Lower Hutt 5040, New Zealand

[4]College of Earth, Ocean, and Atmospheric Sciences, Oregon State University, Corvallis, OR 97331, USA

[5]Now at U.S. Naval Research Laboratory, John C. Stennis Space Center, MS, USA

[6]University of Auckland, School of Environment, Private Bag 92019, Auckland 1142, New Zealand

[7]Now at Texas A&M University Corpus Christi, 6300 Ocean Drive, Corpus Christi, TX 78412, USA

Submitted to G^3: Geochemistry, Geophysics, Geosystems

18 July 2023

Keywords

gas hydrate, seismic imaging, high-resolution seismic data, seismic inversion, advective heat flow

Key Points

- A distinct gas-hydrate to free-gas transition is mapped using high- and low-frequency seismic data
- Gas and hydrate accumulations in Urutī Basin are controlled by the structural setting, ongoing deep-sourced fluid flow, and near surface stratigraphy
- Regions of high modeled heat flow can be directly related to accumulations of gas and gas hydrate

Abstract

The Hikurangi Margin east of New Zealand's North Island hosts an extensive gas hydrate province with numerous gas hydrate accumulations related to the faulted structure of the accretionary wedge. One such hydrate feature occurs in a small perched upper-slope basin known as Urutī Basin. We investigate this hydrate accumulation by combining a long-offset seismic line (10-km-long receiver array) with a grid of high-resolution seismic lines acquired with a 600-m-long hydrophone streamer. The long-offset data enable quantitative velocity analysis while the high-resolution data constrain the three-dimensional geometry of the hydrate accumulation. The sediments in Urutī Basin dip landward due to ongoing deformation of the accretionary wedge. These strata are clearly imaged in seismic data where they cross a distinct bottom simulating reflection (BSR) that dips, counterintuitively, in the opposite direction to the regional dip of the seafloor. BSR-derived heat flow estimates reveal a distinct heat flow anomaly that coincides spatially with the upper extent of a landward-verging thrust fault. We present a conceptual model of this gas hydrate system that highlights the roles of fault-controlled fluid flow at depth merging into strata-controlled fluid flow into the hydrate stability zone. The result is a layer-constrained accumulation of concentrated gas hydrate in the dipping strata. Our study provides new insight into the interplay between deep faulting, fluid flow and the shallow processes involved in gas hydrate formation.

Plain language summary

Gas hydrates are ice-like substances in which natural gas molecules are trapped in a cage of water molecules. They exist where the pressure is high, temperature is cold, and enough methane is present. These conditions exist in the marine environment at water depths greater than 300-500 m near sediment-rich continental margins and in polar regions. It is important to study gas hydrates because they represent a significant part of Earth's carbon budget and influence the flow of methane into the oceans and atmosphere. In this study we use the seismic reflection method to generate images of gas-hydrate-bearing marine sediments east of New Zealand. Our data reveal an intriguing relationship between deep-sourced fluid flow upward along a tectonic fault, and shallower flow through dipping sediments. This complex fluid flow pattern has led to disruption of the gas hydrate system and the formation of concentrated gas hydrate deposits within the dipping sediments. Our study highlights an

64 important interplay between relatively deep tectonic processes (faulting and fluid flow) and
65 the shallow process of gas hydrate formation.
66

67 ## Introduction

68 **Gas hydrate and seismology**

69 Gas hydrate, a solid clathrate compound of water and gas that is widespread on
70 continental slopes, is a significant component of the global carbon cycle and plays a role in
71 dynamic slope processes [e.g., *Sloan*, 2003]. Gas hydrate stability is primarily governed by
72 (high) pressure and (low) temperature but is also affected by gas composition and pore water
73 salinity. For hydrate to form, gas must be present in concentrations that exceed solubility at
74 the local temperature and pressure. Suitable conditions for gas hydrate occurrence are
75 generally restricted to continental slopes and polar regions [e.g., *Kvenvolden et al.*, 1993].
76 Initial identification of gas hydrate systems is typically undertaken using active source multi-
77 channel reflection seismology. In seismic data, gas hydrate occurrences are generally inferred
78 from observations of a bottom-simulating reflection (BSR) that usually occurs in shallow
79 sediments at the expected depth of the base of gas hydrate stability (BGHS). As such, the BSR
80 is interpreted to represent the transition from free gas in the pore space below the BGHS to
81 gas hydrate within the pore space above it [*Shipley et al.*, 1979]. Departures from the
82 expected depth can be used to infer lateral variations in apparent heat flow resulting from
83 fluid advection. In this paper we analyze a uniquely imaged gas hydrate system along a part
84 of the Hikurangi margin, New Zealand, to better understand the relationship between
85 tectonic structure, stratigraphic controls, and fluid advection that focus gas hydrate
86 formation.

87 The frequencies contained in a propagating seismic wave affect the resolution of the
88 seismic data. Many seismic evaluations of gas hydrate accumulations have been undertaken
89 using conventional hydrocarbon exploration techniques, which often focus on deeper
90 reservoir units using seismic sources with power and frequency properties appropriate for
91 these targets. However, lower-power, higher-frequency sources have also been used for
92 targeted hydrate studies because only shallower penetration depths are necessary [e.g.,
93 *Haines et al.*, 2017; *Tréhu et al.*, 2004; *Vanneste et al.*, 2001; *Wood et al.*, 2008]. Such
94 investigations have found that gas hydrate systems can have a distinct frequency-dependent

response that causes the BSR to decrease in amplitude or disappear altogether with increasing frequency [e.g., *Vanneste et al.*, 2001]. This phenomenon is possibly the result of the base of hydrate stability being a transitional rather than a distinct boundary, with the base of hydrate occurring some distance above the actual base of hydrate stability [e.g. *Nole et al.*, 2018] as a result of the processes that are required to convert gas (primarily methane) and pore water into hydrate [*Clennell et al.*, 1999].

The analysis of seismic amplitude variations with offset (AVO) enables better constraints on sedimentary properties (e.g., lithology, petrology, porosity, permeability), pore fluids (e.g., gas, oil, water), and hydrate occurrences within a hydrate setting [*Ecker et al.*, 1998]. However, analysis of an AVO response requires observations over a sufficiently wide range of source-receiver offsets. Hydrocarbon exploration data are often suitable for such an approach, but short-offset lower-power higher-frequency surveys conducted specifically for shallow-penetration hydrate characterization are often insufficient for such analyses.

Understanding the effects of acquisition parameters such as source configuration and streamer length on seismic resolution is particularly important when analyzing gas hydrate systems because thin stratigraphic (e.g., porous sandstone or tight shale units) or structural (e.g., fault) features affect fluid migration and hydrate accumulation [*Boswell et al.*, 2012; *Crutchley et al.*, 2015; *Fraser et al.*, 2016; *Fujii et al.*, 2015; *Navalpakam et al.*, 2012; *Tréhu et al.*, 2004], thereby significantly impacting the dynamics of gas hydrate systems. Although there have been informative studies in recent years on the effect of survey acquisition parameters on the seismic response from gas hydrate systems [e.g., *Crutchley et al.*, 2023; *Haines et al.*, 2017], detailed analyses of such complementary datasets are not common.

Geological setting

The Hikurangi Margin is located on an active subduction zone where the Pacific Plate subducts obliquely beneath the Australian Plate off the east coast of New Zealand's North Island (Figure 1). Convergent plate motion decreases from around 45 mm/yr at the northern end of the margin to around 41 mm/yr at the southern end, due to counter-clockwise rotation of the relative plate motion vectors [*Barnes et al.*, 2010; *De Mets et al.*, 1994]. Convergence along the plate interface accommodates roughly 85% of the plate-normal motion [*Nicol and Beavan*, 2003]. The remainder of plate-normal motion and the majority of plate-parallel motion (~60%) is accommodated within the overriding accretionary wedge through a

126 combination of thrust faulting, strike-slip faulting and vertical clockwise rotation [*Nicol and*
127 *Wallace*, 2007]. The thrust imbricated frontal wedge of the Hikurangi Margin has formed
128 against a backstop of Mesozoic Torlesse basement [*Barnes et al.*, 2010; *Bland et al.*, 2015;
129 *Lewis and Pettinga*, 1993]. Thrust faults that extend from the subduction interface into the
130 wedge result in a series of NE-trending anticlinal ridges separated by slope basins that
131 accumulate younger sediment.

132 An extensive gas hydrate province on the Hikurangi Margin has been investigated by
133 regional seismic studies [e.g., *Henrys et al.*, 2003] that have led to more detailed investigations
134 and a better understanding of focused hydrate accumulations, often occurring in regions of
135 focused fluid flow within the accretionary margin [*Crutchley et al.*, 2011; *Crutchley et al.*,
136 2023; *Crutchley et al.*, 2021; *Fraser et al.*, 2016; *Pecher et al.*, 2004; *Pecher et al.*, 2010; *Plaza-*
137 *Faverola et al.*, 2012; *Plaza-Faverola et al.*, 2014; *Turco et al.*, 2020].

138 The focus of this paper is an intriguing, locally focused gas hydrate system within Urutī
139 Basin (Figures 1 and 2), around 40 km SE of Castlepoint on the coast of the North Island. The
140 distinctive Palliser-Kaiwhata strike-slip fault (Figure 1) cuts obliquely through this region of
141 the wedge, with a local releasing bend on Urutī Ridge [*Barnes et al.*, 1998; *Barnes et al.*, 2010].
142 The basement beneath Urutī Basin consists of rocks from the Hikurangi Plateau, which is a
143 large Early Cretaceous basaltic oceanic province comprised mostly of volcaniclastic and
144 extrusive volcanic deposits [*Mortimer and Parkinson*, 1996]. Above the basement, the
145 imbricated wedge has a foundation of pre-subduction passive margin Cretaceous-Paleogene
146 rocks in which the décollement is located. These rocks are overlain by Miocene to Recent
147 cover and slope basin sediments. Dredge samples T119 and V479 from the eastern forelimb
148 of Urutī Ridge show that the ridge contains early to middle Pliocene indurated mudstones
149 [*Barnes et al.*, 2010]. Urutī Basin sediments were deposited simultaneously with uplift of Urutī
150 Ridge; however, no sediment samples have yet been collected from the basin.

151 **Study outline**

152 In early 2010, the Urutī Basin gas hydrate system was imaged during the PEG09
153 petroleum exploration seismic survey (Figures 1 and 2). Urutī Basin contains many seismic
154 characteristics of an active gas hydrate system such as prominent BSRs and enhanced
155 reflections above and below the BSR that may correspond to hydrate or gas accumulations
156 [*Fraser et al.*, 2016]. *Fraser et al.* [2016] identified a highly reflective possible hydrate-bearing

layer within the hydrate stability zone overlying a set of strong reflections beneath the BSR that probably correspond to gas-charged strata. This gas hydrate system was targeted and imaged by the higher-resolution RR1508-HKS02 survey in 2015.

In this paper, we analyze and compare co-located PEG09 and RR1508-HKS02 seismic data over the gas hydrate system to:

1. interpret the distribution of gas hydrate and underlying gas in this region,
2. investigate the effects of seismic frequency on the imaging of a focused gas hydrate system to better understand the stratigraphic, structural and dynamic controls that lead to specific configurations of hydrate and gas, and
3. evaluate enhanced fluid advection through a gas hydrate system using BSR-derived heat flow estimates.

We found that the relationship between stratigraphy, faulting, and fluid flow can provide critical insight into processes controlling gas hydrate formation.

Methods

Data acquisition

The PEG09 survey was conducted in 2009-2010 by Reflect Geophysical with the *MV Reflect Resolution* under contract from the New Zealand government as part of a regional conventional hydrocarbon exploration study. The acquisition system included three Bolt APG 8500s airguns and a 10,000-m-long 800-channel (12.5 m group interval) hydrophone streamer towed at an approximate depth of 11 m [*RPS Energy Pty Ltd*, 2010]. Shot spacing was 37.5 m for a nominal fold of roughly 133.

In June 2015, the RR1508-HKS02 seismic reflection survey (referred to henceforth as the HKS02 survey) was collected aboard the *RV Roger Revelle* during voyage RR1508. This survey incorporated a high-resolution short-offset acquisition system including two 45/90 cu. in. generator-injector (GI) airguns and a 600-m-long 48-channel (also 12.5 m group interval) hydrophone streamer towed at a depth of approximately 3.5 m with a shot spacing of 25 m for a nominal fold of 12.

Seismic processing

The seismic data in the vicinity of Urutī Ridge have been processed with the aim of maximizing resolution of the shallow gas hydrate system while preserving true relative amplitudes. Processing of seismic lines PEG09-25 and HKS02-01 to -06 aimed to minimize the

introduction of differences in the stacked data resulting from the greatly different offset ranges in the two datasets. Due to the effects of streamer feathering and limited constraints on the HKS02-01 receiver positions, shot and receiver positions between the two co-located profiles differ slightly (<100 m). To counter this, the CMP positions for the surveys were set to be along straight coincident lines with a common CMP spacing of 6.25 m. Time shifts accounted for a start-of-trace delay and acquisition depth. Based on frequency analysis of the CMP gathers, trapezoidal bandpass filters of 5-10-50-60 and 12-35-160-210 Hz were applied to the PEG09-25 and HKS02 datasets, respectively, to attenuate low- and high-frequency noise. To correct for spherical divergence, a recovery function of $t \times v_{RMS}(t)^2$ was applied to both datasets, where t is two-way-time and v_{RMS} is the root-mean-square velocity derived from semblance-based velocity analysis of the PEG09-25 data. Spherical divergence gain recovery was preferred over automatic gain corrections as it preserves relative amplitude information. Pre-stack Kirchhoff time migration was then applied to both datasets and a phase shift of 180° was applied to the HKS02 lines to match the PEG09 lines, assuming a zero-degree positive American polarity convention, e.g., at the seafloor (Figure 3A and B). Instantaneous amplitude (Figure 3C and D) and instantaneous frequency (Figure 3E and F) attributes provide visualizations of the data that emphasize contrasts in physical properties and stratigraphic bedding scales, respectively.

Pre-stack AVO Inversion

To characterize the fine-scale structure, we carried out AVO seismic inversion, which requires a low frequency impedance model (a background model) as input. Typically, background trends of P-wave impedance, density, etc. are constrained by well data, but due to the absence of wells in the study area, we derived pseudo-wells from our stacking velocity model. Densities were determined using Gardner's relationship between P-wave velocity and bulk density [*Gardner et al.*, 1974].

To determine the S-wave velocity, the Krief equation [*Krief et al.*, 1990] was used below the BSR with coefficients set for a matrix of sandstone with gas as the pore fluid. Outside the gas charged units, it was not possible to use the Krief equation for wet sandstone as the equation breaks down at these shallow depths in lower-velocity units that are not fully lithified; hence Castagna's "mud rock" equation was used [*Castagna et al.*, 1985].

Pre-stack AVO inversion was tested at the pseudo-well locations (every 100th CMP) to validate the input parameters for robustness before inverting the whole seismic section. A typical correlation factor of 0.98 between the real (input data) and synthetic data was achieved for the pseudo wells [*Fraser*, 2017]. P-impedance, Z_P, S-impedance, Z_S and V_P/V_S were computed for Urutī Basin data. The V_P/V_S ratio is more sensitive to a change in fluid type than V_P or V_S alone.

Heat flow

To investigate the role of fluid advection through the gas hydrate system, apparent heat flow was derived from the BSR using a simple conductive model [*Henrys et al.*, 2003; *Shankar et al.*, 2010; *Townend*, 1997]. This technique involves calculating the thermal gradient from the observed BSR depth below seafloor assuming that the BSR marks the free gas to hydrate phase conversion for a particular gas composition. The thermal gradients thus derived can be converted to heat flow by estimating the thermal conductivity. Gridded horizon depths (i.e., seafloor and BSR) were extracted from depth-converted sections to account for the effect of variable velocity (1500-2000 m/s) in the shallow seafloor on travel time.

The seafloor temperature, T_{sf}, was derived by extrapolating downward from the lower part of a nearby expendable bathy-thermograph (XBT) drop (drop HKS02-22) collected at the site [*Baker*, 2016]. Temperature at the sea floor as function of water depth, $T_{sf}(d_{sf})$, for these data was thereby estimated to be:

$$T_{sf}(d_{sf}) = 8.3°\mathrm{C} - d_{sf}\,(0.0064°\mathrm{C})$$

where d_{sf} is seafloor depth. Pressure at the BSR, P, was assumed to be hydrostatic in agreement with other studies in the region [e.g., *Henrys et al.*, 2003; *Pecher et al.*, 2010].

Gas hydrate phase boundary conditions approximated at the BSR were used to determine the temperature at the BSR, T_{BSR}, using the relationship of [*Bouriak et al.*, 2000] for a methane-seawater system. This formulation assumes a gas composition of 100% methane and a standard sea-water salinity of 34 PSU. Gas composition is consistent with previous analyses on the southern Hikurangi Margin [*Koch et al.*, 2016; *Schwalenberg et al.*, 2010a; *Schwalenberg et al.*, 2010b].

Assuming a constant geothermal gradient between the seafloor and the BSR, the geothermal gradient, G, was calculated using:

$$G = \frac{T_{BSR} - T_{sf}}{d_{sed}}$$

where d_{sed} is the sediment thickness between the seafloor and the BSR.

To calculate heat flow, the thermal conductivity of the system, κ, was estimated to be 1 W/m°C [cf. *Henrys et al.*, 2003; *Townend*, 1997] using Hamilton's [1978] porosity-depth relationship for near surface terrigenous sediments and the geometric mean conductivity-porosity relationship of Woodside and Messmer [1961]. This allowed heat flow values, H, to be calculated using the simple conductive heat transport relationship:

$$H = \kappa G$$

Heat flow values were then gridded using a flex gridding algorithm. Townend [1997] corrected for sedimentation rates and found there to be significant changes in heat flow values, with high sedimentation rates having a dampening effect on uncorrected heat flow values. However, since sedimentation rates are largely unknown in Urutī Basin, heat flow maps were left uncorrected, a stance also taken by Henrys et al. [2003]. Additionally, because we are concerned with differences in heat flow within a localized region, a sedimentation rate correction is less important since it should be similar across the region of interest.

Results

Seismic Observations

Comparison of these two datasets requires a consideration of resolution limitations. In simple terms, the minimum resolvable thickness of a layer is generally accepted to be a quarter of the wavelength [*Yilmaz*, 1987]. This gives a minimum resolvable thickness of 14 m for PEG09 compared to 7 m for HKS02 using a peak frequency of 29.3 Hz for PEG09 and 60.5 Hz for HKS02 and a seismic velocity of 1680 m/s. Peak frequencies were obtained from frequency spectra extracted from the upper 0.75 s of basin sediment. Lateral resolution is related to the Fresnel Zone, which describes the portion of a reflector where reflected waves interfere constructively [*Yilmaz*, 1987]. For example, for an arbitrary reflection at 1.9 s (the approximate position of the BSR) with an average velocity of 1530 m/s, the first Fresnel Zone diameter would be 195 m for PEG09 and 136 m for HKS02. The Fresnel Zone increases (and therefore lateral resolution decreases) with increasing depth. Although migration tends to collapse the Fresnel Zone to roughly the dominant wavelength (52 m for PEG09 and 25 m for HKS02) in the inline direction [*Stolt and Benson*, 1986], lateral resolution in the offline direction will be relatively low.

Seismic lines PEG09-25 and HKS02-01 show similar representations of the gas hydrate system in Urutī Basin (Figure 3A and B; position indicated by box in Figure 2). Note several strong reflections, interpreted to correspond to gas charged layers, beneath an inclined BSR that is found beneath a relatively horizontal seafloor. The strongly reflective unit above the BSR is interpreted to be a porous layer (or layers) hosting concentrated hydrate. This reflectivity pattern is typical for layer-constrained systems of hydrate overlying free gas observed elsewhere [e.g., *Boswell et al.*, 2012].

Seismic attributes provide further information to assist with the interpretation of the two seismic datasets. Instantaneous amplitude images of the high- and low-frequency data (Figure 3C and D) show enhanced amplitudes associated with the horizon inferred to be a porous layer hosting gas hydrate within the hydrate stability zone and charged with free gas below the BSR. As expected, the thickness of high-amplitude layers is generally greater in the low-frequency data, suggesting that bed-thickness tuning effects should be taken into consideration when assessing individual gas zones in the region. Simple wedge models following the method of *Hamlyn* [2014] suggest that that the thickness at which two events become indistinguishable, for a single hydrate-bearing layer, is around 15.0 m for the PEG09 dataset and 4.5 m for the HKS02 dataset [*Baker*, 2016]. Instantaneous frequency images (Figure 3E and F) highlight the background stratigraphy, indicating that it is laterally continuous in the vicinity of Urutī Basin anomaly. Lower frequencies probably correspond to regions of gas charging which would tend to attenuate the frequency content in the signal passing through it.

Hydrate and gas distributions evaluated by inversion

AVO inversion of the 2D seismic data from transect PEG09-25 [*Fraser*, 2017] (Figure 4) provides a means to constrain sedimentary pore space content (i.e., water, gas, hydrate) in a gas hydrate setting [*Dutta and Dai*, 2009; *Fohrmann and Pecher*, 2012]. However, the lack of well control here requires the introduction of some assumptions concerning the background lithology and stratigraphy based on regional interpretations of sediment types and accumulation patterns [e.g., *Barnes et al.*, 2010; *Kroeger et al.*, 2015]. Despite the ambiguities resulting from the lack of definitive lithological controls, the processed seismic images, seismic attributes, and AVO inversion results are consistent with a gas hydrate system associated with a high-porosity, high-permeability sandstone unit.

Beneath the BSR, an area of low V_P/V_S ratio suggests the presence of gas (Figure 4D). Within this region is a distinct horizon of high impedance (Figure 4B and C) which appears to be stratigraphically continuous with a relatively high impedance layer above the BSR and is parallel to the overall stratigraphic trend. Above the BSR, high P- and S-wave impedance horizons (Figure 4B and C) that corresponds to the interpreted hydrate-bearing layer (Figure 4A) may represent stratigraphically controlled hydrate deposits. These inversion results support the idea of localized fluid flow affecting the depth of the BSR, with at least one low-permeability horizon with high impedance helping to channel the flow of gas from below, leading to the accumulation of hydrate within the hydrate stability zone. An upward flexure of the BSR, indicative of higher heat flow, is consistent with this interpretation. As the BSR does not appear as a distinct stand-alone reflection in any of the images, it is unlikely to be the result of a wide-spread free gas accumulation, but rather is indicative of the transition from free gas to lack of free gas in permeable strata.

Regional configuration of the focused hydrate accumulation

The closely spaced network of parallel HKS02 2D seismic lines, spanning a distance of about 7 km along Urutī Ridge and Basin and collected in the area of the hydrate anomaly on PEG09-25 (Figure 5), enable a preliminary assessment of the 3D structure of the feature. The four parallel seismic lines (HKS02-01 to -04) each show: (1) bright reflections below the BSR corresponding to gas charged sediments, (2) an inclined and irregular BSR that in places shallows toward land under a relatively flat seafloor, and (3) a positive polarity reflection (of variable strength) within the hydrate stability zone interpreted to be a hydrate charged layer.

The width and height of the interpreted hydrate accumulation increases from southwest (950 m long and 75 ms high at line HKS02-04) to northeast (2500 m long and 218 ms high line HKS02-02), suggesting that the northeastern extent of the feature has not been imaged (Figure 6). Also, the maximum uplift of the BSR (measured above the regional BSR to the southeast below the hydrate anomaly) increases from <10 ms on HKS02-04 (Figure 5D) in the southwest to about 100 ms on HKS02-02 in the northeast (Figure 5A). The region of most pronounced BSR uplift imaged in Line HKS02-02 is underlain by a relatively broad (~2 km wide) region of suppressed amplitudes and acoustic turbidity (Figure 5A). This zone of suppressed amplitudes coincides with the upper extent of the backthrust interpreted by *Bland et al.* [2015] (Figures 2 and 3).

342 **Heat flow implications of the uplifted BSR**

343 Heat flow estimates based on the regional interpretation of the BSR reveal a distinct
344 heat flow anomaly in the vicinity of Urutī Basin hydrate anomaly (Figure 6). Heat flow is
345 modelled to rise from a local background of about 37 mW/m^2 to a maximum of about
346 45 mW/m^2 just landward of the intersection of the hydrate anomaly with the regional BSR.
347 The upper extent of the backthrust (Figures 3 and 6) coincides with the position of the heat
348 flow anomaly (Figure 6). Additionally, the most laterally extensive (i.e., broadest) region of
349 the gas hydrate anomaly (imaged on Lines HKS02-01 and HKS02-02) lies updip (i.e., to the
350 southeast) of the most pronounced region of the heat flow anomaly.

351 **Data resolution considerations**

352 Consideration of the resolution of the high- and low-frequency datasets enables a
353 number of features to be considered more fully. First, notice the amplitude and phase
354 characteristics of the concentrated hydrate reflection (Figure 3). In both the low- and high-
355 frequency data, the reflection manifests as a single high-amplitude positive wavelet, so the
356 reflection in the high-frequency data occupies less volume (is thinner) than in the low-
357 frequency data. Second, consider the effect of resolution on layers within the gas zone. The
358 reflective region below the BSR that is interpreted to be gas charged appears to be more
359 homogeneous in the low-frequency data than in the high-frequency data where the gas
360 appears to occur in layers that are more distinct and spread out from each other. This finding
361 suggests that the interpreted continuity of the BSR depends on the wavelength of a reflecting
362 wave compared to the thickness of layers crossed by the BSR, and is consistent with previous
363 work that has found the observed continuity of a BSR being affected by the frequency content
364 of the seismic data [e.g., *Papenberg*, 2004; *Wood and Gettrust*, 2001]. Details of the
365 stratigraphy are also much clearer in the high-frequency data; for example, minor erosional
366 surfaces, pinch outs and possible mass flow deposits can be seen better in the high-frequency
367 data (Figure 3B).
368

369 ## Discussion

370 **Controls on the depth of the BSR**

371 The PEG09-25 and HKS02 seismic data support the interpretation of upwelling fluids,
372 probably from several km depth in the accretionary wedge, that are channeled upward along

deep-seated faults (i.e., the backthrust, Figure 2) to terminate in younger sediments just below the BSR (Figures 2 and 3). The advection of warm fluids at a focused location can result in lateral variability of heat flow, thereby causing a localized uplift in the base of gas hydrate stability [e.g., *Zwart et al.*, 1996]. As mentioned previously, the location of greatest modeled heat flow coincides with the updip termination of the underlying backthrust (Figure 6).

There is a very narrow range of transport rates that can lead to an observable effect on the BSR – too low and there is no visible effect, too high and the BSR is no longer identifiable (i.e. the stability boundary is at or near the seafloor) [*Bredehoeft and Papaopulos*, 1965; *Pecher et al.*, 2010]. Using the method of *Tréhu et al.* [2003], we modelled a range of steady-state flow scenarios that are consistent with our observations at Urutī Basin (Figure 7). In our models we used the temperature solution of *Bredehoeft and Papaopulos* [1965] which depends on a given thickness, L, of the upward flow zone (set somewhat arbitrarily to 2000 m here, corresponding to deep-seated faulting within the accretionary margin)

$$T(z) = T_{BGHS} + (T_L - T_{BGHZ})\frac{e^{\frac{\beta}{L}z} - 1}{e^{\beta} - 1}$$

where

$$\beta = \frac{\emptyset \rho_w c_w v_z}{\kappa_m}.$$

T_{BGHS} is the temperature at the base of the gas hydrate stability zone, T_L is the temperature at the base of the upward flow zone, ϕ is the porosity of the sediments, ρ_w is the fluid density, c_w is the fluid heat capacity, κ_m is the thermal conductivity of the matrix, and v_z is the vertical flow rate. Our conductive background thermal model uses temperatures at the seafloor and base of the hydrate stability zone of 4°C and ~17°C [based on *Bouriak et al.*, 2000], respectively. Assuming a thermal gradient of 0.037°C/m, consistent with the regional BSR-derived heat flow, predicts that the base of the hydrate stability zone, z_0, is ~350 m below the seafloor, and T_L at a depth of 2350 m below the seafloor will be ~91°C (Figure 7). Other parameters used for these models were ϕ = 0.33, ρ_w = 1024 kg/m^3, c_w = 4180 J/kg°C, and κ_m = 1 W/m°C, to be consistent with *Pecher et al.* [2010].

Our mapping at Urutī Basin shows a difference in heat flow of ~8 mW/m^2 between the peak heat flow and background (Figure 6), and assuming a thermal conductivity of 1 W/m°C [*Harris et al.*, 2019], corresponds to an enhancement of the thermal gradient of ~0.008°C/m due to the flow. A vertical fluid flow rate of about 1 mm/yr generates a shallow thermal

403 gradient of 0.045°C/m (Figure 7) consistent with the seafloor BSR derived thermal gradient at
404 the fault. Furthermore, assuming a roughly constant temperature of 17°C at the base of
405 hydrate stability that is deflected upward by fluid flow suggests that the BGHS would have
406 risen from 350 m to 280 m below the seafloor, which is broadly consistent with the seismic
407 images of the deflected BSR at Urutī Basin (Figure 5). Note that the thickness chosen for the
408 upward flow zone in our model affects the derived flow rates. A shallower source for the fluid
409 would result in cooler temperatures and higher vertical flow rates to generate the same
410 anomaly.

411 The AVO inversion results show that the shallow stratigraphy in Urutī Basin also
412 contributes to focused fluid flow in this setting. The 3-4 km wide region of low P-wave
413 impedance (Figure 4B), high S-wave impedance (Figure 4C) and low Vp/Vs (Figure 4D) under
414 the BSR is interpreted to be a zone of gas-charged pore space immediately above the upper
415 termination of the deep-seated fault. However, several landward-dipping strata within this
416 region exhibit P- and S-wave impedances that are markedly higher than the background
417 values. This difference supports a geological (i.e., properties related to lithology or porosity)
418 rather than a pore fluid origin for such layers. One probable interpretation is that these high
419 impedance layers correspond to tight shale units – under which gas-charged fluids have
420 travelled updip through a porous and permeable layer into the overlying GHSZ.

421 **Constraining a hydrate reservoir unit**

422 Accurate determinations of hydrate distributions and concentrations require the
423 identification and characterization of stratigraphic units that can host hydrate or free gas (or
424 other fluids). The quality of such reservoir units depends on their ability to store and deliver
425 the material that they host [*Grier and Marschall*, 1992]. Storage capacity is determined by the
426 volume of interconnected pores (effective porosity) in a reservoir unit, whereas deliverability
427 is a function of a unit's permeability. Within Urutī Basin, several seismically mappable
428 horizons are interpreted to correspond to high-quality reservoir units due to their enhanced
429 amplitudes (and impedance contrasts) within the gas zone beneath the BSR (Figures 4 and 5).
430 By extension, these same units also could be capable of hosting elevated concentrations of
431 gas hydrate within the hydrate stability field above the BSR, with the rationale that significant
432 hydrate growth relies on large interconnected pore spaces [e.g., *Torres et al.*, 2008; *Uchida et*
433 *al.*, 2004]. However, seismic amplitudes alone are not enough to adequately constrain

porosity and permeability. Even low gas saturations, if evenly distributed through the pore spaces within a layer, can significantly decrease seismic impedance and enhance reflection amplitudes [e.g., *Domenico*, 1976].

The distinct high-amplitude feature above the BSR in Urutī Basin is interpreted to result from a high-quality reservoir unit hosting a concentrated gas hydrate accumulation (labelled 'hydrate' in Figure 4A). Based on assessments of the stratigraphic setting, the stratigraphic configuration here probably consists of sand-dominated layers interbedded with mud-dominated units within a turbidite sequence [*Barnes et al.*, 2010; *Kroeger et al.*, 2015]. This configuration of interbedded sands and shales is interpreted to cause the observed segmentation of the BSR: sandy stratigraphic units promote elevated gas and gas hydrate saturations causing high-amplitude BSR segments, and muddy units inhibit gas and gas hydrate accumulation resulting in weak and absent BSR segments. The high-amplitude feature extends to variable distances above the BSR (Figure 5 and blue highlighted regions in Figure 6). Interpolating between these positions, the reservoir units are observed to cover an area of about 13 km^2; however, there are no constraints to the NE or SW, so the full spatial extent of the feature remains poorly constrained.

Estimates of hydrate saturation in Urutī Basin as imaged with seismic line PEG09-25 have been made by *Baker* [2016] who calculated saturations of 39% to 52% assuming clay fractions of 10% to 90% [*Lee and Deming*, 2002]. Additional calculations of gas hydrate concentrations in the Pegasus Basin for a range of targets investigated by *Fraser et al.* [2016] and *Crutchley et al.* [2016] give values of 49% to 56% and 32% to 51% for clay fractions of 10% to 90%. A more theoretical basin-wide approach to the estimation of hydrate concentrations was made by *Kroeger et al.* [2015] who predicted that concentrations over 50% would be found in some areas, in agreement with the previous estimates.

High hydrate concentrations such as those calculated above – and manifested as mappable amplitude anomalies within the hydrate stability zone – appear to be restricted to a few layers within the part of Urutī Basin imaged by our data. The seismic data suggest that a combination of factors has led to the establishment of this feature. These include: (1) the presence of a regionally extensive high-quality sand-dominated layers with sufficient porosity and permeability to both facilitate migration of fluids containing natural gas and act as a host for gas hydrate, (2) the superposition of a low-permeability sealing layer that acts as a barrier

for vertical fluid flow and facilitates up-dip flow in the permeable strata below, and (3) a source of fluid flow from below providing gas to the system (Figure 8).

In Figure 8 we conceptualize the key processes leading to the concentrated gas hydrate accumulation, starting with fault-controlled fluid flow, and culminating in stratigraphically controlled gas migration into the gas hydrate stability zone. The presence of numerous strata with sufficient porosity is indicated by several highly reflective horizons within the gas charged region. However, the seismic data show that just the one main horizon appears to continue as a high-amplitude (flipped polarity), high-hydrate-concentration feature within the hydrate stability zone. We interpret that this layer is capped by a sealing unit that acts as a barrier for gas transport from below. The intersection of the good sealing unit with the BGHS results in fluids travelling along the underlying porous and permeable bed.

Combining the extent of the high-amplitude hydrate anomaly in seismic data (Figure 5, and indicated by the blue line segments in Figure 6) and the modelled heat flow based on BSR depth (Figure 6) shows a link between higher heat flow and the lateral extent of the hydrate anomaly. The greatest heat flow is observed along the northeastern extent of the backthrust in the mapped region, coinciding with the most extensive hydrate anomaly on lines HKS02-01 and HKS02-02. The lowest heat flow is observed along the SW side, corresponding to the shortest hydrate anomaly on line HKS02-04. Since the full regional extent of the upward deflected BSR anomaly has not been mapped by the available seismic data, it is likely that anomalously high heat flow – and therefore hydrate accumulation within the stratigraphically controlled horizon described above – continue to the NE.

Conclusions

An intriguing gas-hydrate anomaly observed in seismic reflection data from Urutī Basin is characterized by a high-amplitude reflection extending up into the hydrate stability field from an uplifted BSR. The application of AVO inversion methods supports the presence of concentrated gas hydrate reservoir units within the basin. A grid of high-resolution seismic data shows that the structure of this feature is 3D in nature and significantly affects seafloor heat flow, interpreted to be the result of focused fluid transport from a deep-seated backthrust underlying the basin. Mapping of the extent of the hydrate feature relative to seafloor heat flow (estimated using the depth of the BSR) shows that regions of enhanced

heat flow – and therefore enhanced fluid flow – coincide with a more laterally extensive hydrate anomaly. The spatial relationship between the interpreted hydrate anomaly and the underlying gas-charged region suggests that ongoing fluid flow plays a significant role in sustaining accumulation of gas hydrate within porous and permeable units. The available data are insufficient to constrain the full spatial extent of the system, so our estimate of the areal extent of the reservoir units is likely to represent a lower bound.

Acknowledgments

We thank the captain and crew of the *RV Roger Revelle* (cruise RR1508) for their assistance in collecting seismic data presented here. The National Science Foundation funded Harris and Tréhu for this cruise through grant OCE1355878. Harris was also supported by NSF-OCE1753665. New Zealand Petroleum and Minerals provided data associated with the PEG09 seismic survey. All seismic data were processed using an academic license to the University of Otago for GLOBE Claritas. A Hampson and Russel (CGG) academic license was used for AVO and inversion analysis. Hamish Bowman is thanked for his technical assistance with computing and mapping. Additional funding for this project was obtained from the New Zealand Ministry for Business, Innovation and Employment research programme C05X1204. Baker and Fraser were supported by University of Otago MSc and PhD scholarships, respectively. Manuscript preparation was facilitated by a sabbatical visit for Gorman to GEOMAR in Kiel.

Data availability statement

Bathymetric, heat flow, water column temperature, raw seismic data and all other underway data from RV Roger Revelle voyage RR1508 are available at https://www.marine-geo.org/tools/new_search/search_map.php?&a=1&entry_id=RR1508&output_info_all=on . The calculated heatflow grid shown in Figure 6 and associated ascii files along with all processed seismic data used for this study are available from DOI: 10.5281/zenodo.8152964 .

Figures

Figure 1. Urutī Basin study area on Hikurangi Margin southeast of New Zealand's North Island showing seismic data locations over accretionary ridges and basins. Bathymetric data courtesy of Land Information New Zealand cruise TAN1307 [*Crutchley et al.*, 2015]. Inset map shows general plate tectonic and bathymetric setting of the region with continental crust underlying relatively shallow ocean in light green shades and oceanic crust under deeper ocean in shades of darker blue. Region of interest highlighted in Figure 6 is indicated by a grey box. Segments of seismic lines shown in Figure 5 are highlighted in yellow.

Figure 2. PEG09-25 regional schematic structural interpretation simplified from *Bland et al.* [2015] highlighting the series of faulted ridges on the Hikurangi accretionary margin. Bottom simulating reflections are indicated by broken yellow lines. Extent of seismic data in Figure 3 within Urutī Basin indicated by pink box. Interpreted Urutī Basin backthrust highlighted in red.

Figure 3. Urutī Basin hydrate anomaly in low- (left side) and high-frequency (right side) seismic data. See text for description of specific features labelled in A. In all images, the top of the deep-seated fault beneath Urutī Basin (Figure 2) is indicated. Horizontal and vertical scales are identical in all sub-figures. **A**. PEG09-25 "low frequency" (5-10-50-60 Hz trapezoidal bandpass filter) seismic image. Position of BSR indicated with grey arrows. Position of hydrate-bearing layer (labelled "hydrate") and gas accumulations are indicated. Note the flip in polarity of the hydrate bearing layer as it crosses the BSR: beneath the BSR the reflection is red-black-red (positive-negative-positive), while above the BSR it is black-red-black (negative-positive-negative). **B**. HKS02-01 "high frequency" (12-35-160-210 Hz trapezoidal bandpass filter) seismic image. Examples of features imaged more clearly by the high-frequency data are labeled. **C**. PEG09-25 instantaneous amplitude. **D**. HKS02-01 instantaneous amplitude. **E**. PEG09-25 instantaneous frequency. **F**. HKS02-01 instantaneous frequency.

Figure 4. Pre-stack AVO inversion results from PEG09-25. **A.** Grey-scale image of seismic data from area of interest (cf. Figure 3A) highlighting the hydrate anomaly at Urutī Basin with the background (long-wavelength) seismic velocity model overlain in color. Vertical grey lines show locations of 1D velocity functions that have been interpolated and smoothed to produce the input model for AVO inversion. **B**. P-wave impedance (Z_p). **C**. S-wave impedance

555 (Z_s). **D**. V_p/V_s. See text for discussion of results. Note, horizontal and vertical scales are
556 identical in all subfigures.

557 **Figure 5**. 2.5-D characterisation of Urutī Basin hydrate anomaly. Seismic images for lines
558 HKS02-02, 01, 03, and 04 (see Figure 1 for locations) show changes in reflective units from
559 line to line across about 7 km of the basin. The broken blue line is the interpreted base of gas
560 hydrate stability (or BSR), mainly identified by the upper termination of high-amplitude (gas-
561 charged) layers.

562 **Figure 6**. Heat flow calculated over Urutī Basin (colored surface) with structure contours
563 (0.1 s intervals) shown for the underlying fault surface (as interpreted for line PEG09-25 in
564 Figure 3). The updip termination of the seismically mapped fault (Figures 2 and 3) is shown by
565 the heavy dashed black line. A high heat flow anomaly closely follows the termination of the
566 fault until the termination reaches a depth of around 2.4 s. The sections of the seismic data
567 shown in Figure 5 are highlighted in white, and the lateral extent of the interpreted
568 concentrated hydrate layer is shown in blue. Map projection co-ordinates are NZTM2000 in
569 meters.

570 **Figure 7.** Modeled temperature profiles for various vertically oriented fluid flow
571 scenarios. See text for details of the model. Increased fluid flow results in the temperature
572 profile bulging upward and a shallowing of the base of gas hydrate stability (as shown by
573 indicative depths z_0 to z_4 in the upper left.)

574 **Figure 8**. Cartoon superimposed on a semi-transparent plot of line HKS02-01, showing
575 a proposed mechanism for the uplifted base of gas hydrate stability (BGHS) and the
576 development of a hydrate saturated sedimentary bed within the hydrate stability field. Fluid
577 flow (blue arrows) is focused along a backthrust underlying Urutī Basin and then upward along
578 dipping porous and permeable sedimentary units that cross the BGHS.

579

References

Baker, D. R. (2016), Gas hydrate system dynamics in the Uruti Basin, an upper slope basin on New Zealand's Hikurangi Margin, 141 pp, University of Otago, Dunedin.

Barnes, P. M., B. Mercier de Lépinay, J.-Y. Collot, J. Delteil, and J.-C. Audru (1998), Strain partitioning in the transition area between oblique subduction and continental collision, Hikurangi margin, New Zealand, *Tectonics*, *17*(4), 534-557.

Barnes, P. M., G. Lamarche, J. Bialas, S. A. Henrys, I. A. Pecher, G. L. Netzeband, J. Greinert, J. J. Mountjoy, K. Pedley, and G. J. Crutchley (2010), Tectonic and geological framework for gas hydrates and cold seeps on the Hikurangi subduction margin, New Zealand, *Marine Geology*, *272*(1-4), 26-48.

Bland, K. J., C. I. Uruski, and M. J. Isaac (2015), Pegasus Basin, eastern New Zealand: A stratigraphic record of subsidence and subduction, ancient and modern, *New Zealand Journal of Geology and Geophysics*, *58*(4), 319-343.

Boswell, R., M. Frye, D. Shelander, W. Shedd, D. R. McConnell, and A. Cook (2012), Architecture of gas-hydrate-bearing sands from Walker Ridge 313, Green Canyon 955, and Alaminos Canyon 21: Northern deepwater Gulf of Mexico, *Marine and Petroleum Geology*, *34*(1), 134-149.

Bouriak, S., M. Vanneste, and A. Saoutkine (2000), Inferred gas hydrates and clay diapirs near the Storegga Slide on the southern edge on the Vøring Plateau, offshore Norway, *Marine Geology*, *163*, 125-148.

Bredehoeft, J., and I. Papaopulos (1965), Rates of vertical groundwater movement estimated from the Earth's thermal profile, *Water Resources Research*, *1*(2), 325-328.

Castagna, J. P., M. L. Batzle, and R. L. Eastwood (1985), Relationships between compressional-wave and shear-wave velocities in clastic silicate rocks, *Geophysics*, *50*(4), 571-581.

606 Clennell, M. B., M. Hovland, J. S. Booth, P. Henry, and W. J. Winters (1999), Formation of
607 natural gas hydrates in marine sediments 1. Conceptual model of gas hydrate growth
608 conditioned by host sediment properties, *Journal of Geophysical Research*, *104*(B10), 22,985-
609 923,003.

610 Crutchley, G. J., G. Maslen, I. A. Pecher, and J. J. Mountjoy (2016), High-resolution seismic
611 velocity analysis as a tool for exploring gas hydrate systems: An example from New Zealand's
612 southern Hikurangi margin, *Interpretation*, *4*(1), SA1-SA12.

613 Crutchley, G. J., A. R. Gorman, I. A. Pecher, S. Toulmin, and S. A. Henrys (2011), Geological
614 controls on focused fluid flow through the gas hydrate stability zone on the southern
615 Hikurangi Margin of New Zealand – implications for attractive deposits, *Marine and Petroleum*
616 *Geology*, *28*(10), 1915-1931.

617 Crutchley, G. J., D. R. A. Fraser, I. A. Pecher, A. R. Gorman, G. Maslen, and S. A. Henrys (2015),
618 Gas migration into gas hydrate-bearing sediments on the southern Hikurangi margin of New
619 Zealand, *Journal of Geophysical Research: Solid Earth*, *120*(2), 2014JB011503.

620 Crutchley, G. J., J. I. Hillman, K. F. Kroeger, S. J. Watson, F. Turco, J. J. Mountjoy, B. Davy, and
621 S. Woelz (2023), Both Longitudinal and Transverse Extension Controlling Gas Migration
622 Through Submarine Anticlinal Ridges, New Zealand's Southern Hikurangi Margin, *Journal of*
623 *Geophysical Research: Solid Earth*, *128*(6), e2022JB026279.

624 Crutchley, G. J., J. J. Mountjoy, J. I. T. Hillman, F. Turco, S. Watson, P. B. Flemings, B. Davy, S.
625 Woelz, A. R. Gorman, and J. Bialas (2021), Upward-doming zones of gas hydrate and free gas
626 at the bases of gas chimneys, New Zealand's Hikurangi margin, *Journal of Geophysical*
627 *Research: Solid Earth*, e2020JB021489.

628 De Mets, C., R. G. Gordon, D. F. Argus, and S. Stein (1994), Effect of recent revisions to the
629 geomagnetic reversal time scale on estimates of current plate motions, *Geophysical Research*
630 *Letters*, *21*, 2191-2194.

631 Domenico, S. (1976), Effect of brine-gas mixture on velocity in an unconsolidated sand
632 reservoir, *Geophysics*, *41*(5), 882-894.

633 Dutta, N. C., and J. Dai (2009), Exploration for gas hydrates in a marine environment using
634 seismic inversion and rock physics principles, *The Leading Edge*, *28*(7), 792-802.

635 Ecker, C., J. Dvorkin, and A. Nur (1998), Sediments with gas hydrates: Internal structure from
636 seismic AVO, *Geophysics*, *63*(5), 1659-1669.

637 Fohrmann, M., and I. Pecher (2012), Analysing sand-dominated channel systems for potential
638 gas-hydrate-reservoirs using an AVO seismic inversion technique on the Southern Hikurangi
639 Margin, New Zealand, *Marine and Petroleum Geology*, *38*(1), 19-34.

640 Fraser, D. R. A. (2017), Seismic characterisation of hydrate and shallow gas systems associated
641 with active margin sediments and structures in the Pegasus Basin, Hikurangi Margin, New
642 Zealand, 289 pp, University of Otago, Dunedin.

643 Fraser, D. R. A., A. R. Gorman, I. A. Pecher, G. J. Crutchley, and S. A. Henrys (2016), Gas hydrate
644 accumulations related to focused fluid flow in the Pegasus Basin, southern Hikurangi Margin,
645 New Zealand, *Marine and Petroleum Geology*, *77*, 309-408.

646 Fujii, T., K. Suzuki, T. Takayama, M. Tamaki, Y. Komatsu, Y. Konno, J. Yoneda, K. Yamamoto,
647 and J. Nagao (2015), Geological setting and characterization of a methane hydrate reservoir
648 distributed at the first offshore production test site on the Daini-Atsumi Knoll in the eastern
649 Nankai Trough, Japan, *Marine and Petroleum Geology*, *66, Part 2*, 310-322.

650 Gardner, G., L. Gardner, and A. Gregory (1974), Formation velocity and density—The
651 diagnostic basics for stratigraphic traps, *Geophysics*, *39*(6), 770-780.

652 Grier, S., and D. Marschall (1992), Reservoir quality: Part 6. Geological methods.

653 Haines, S. S., P. E. Hart, T. S. Collett, W. Shedd, M. Frye, P. Weimer, and R. Boswell (2017),
654 High-resolution seismic characterization of the gas and gas hydrate system at Green Canyon
655 955, Gulf of Mexico, USA, *Marine and Petroleum Geology*, *82*, 220-237.

656 Hamilton, E. L. (1978), Sound velocity–density relations in sea-floor sediments and rocks, *The*
657 *journal of the Acoustical Society of America*, *63*(2), 366-377.

658 Hamlyn, W. (2014), Thin beds, tuning, and AVO, *The Leading Edge*, *33*(12), 1394-1396.

659 Harris, R. N., A. M. Tréhu, S. M. Henrys, and A. T. Fisher (2019), Heat Flow data from the
660 Hikurangi subduction margin of New Zealand collected during Revelle STINGS cruise RR1508
661 in 2015, edited, Marine Geoscience Data System.

662 Henrys, S. A., S. Ellis, and C. Uruski (2003), Conductive heat flow variations from bottom-
663 simulating reflectors on the Hikurangi margin, New Zealand, *Geophysical Research Letters*,
664 *30*(2), 1065.

665 Koch, S., H. Schroeder, M. Haeckel, C. Berndt, J. Bialas, C. Papenberg, D. Klaeschen, and A.
666 Plaza-Faverola (2016), Gas migration through Opouawe Bank at the Hikurangi margin offshore
667 New Zealand, *Geo-Marine Letters*, *36*(3), 187-196.

668 Krief, M., J. Garat, J. Stellingwerff, and J. Ventre (1990), A petrophysical interpretation using
669 the velocities of P and S waves (full-waveform sonic), *The Log Analyst*, *31*(06).

670 Kroeger, K. F., A. Plaza-Faverola, P. M. Barnes, and I. A. Pecher (2015), Thermal evolution of
671 the New Zealand Hikurangi subduction margin: Impact on natural gas generation and
672 methane hydrate formation – A model study, *Marine and Petroleum Geology*, *63*, 97-114.

673 Kvenvolden, K. A., G. D. Ginsburg, and V. Soloviev (1993), Worldwide distribution of
674 subaquatic gas hydrates, *Geo-Marine Letters*, *13*(1), 32-40.

675 Lee, Y., and D. Deming (2002), Overpressures in the Anadarko basin, southwestern Oklahoma:
676 Static or dynamic?, *AAPG Bulletin*, *86*(1), 145-160.

677 Lewis, K., and J. Pettinga (1993), The emerging, imbricate frontal wedge of the Hikurangi
678 margin, *Sedimentary basins of the world*, *2*, 225-250.

679 Mortimer, N., and D. Parkinson (1996), Hikurangi Plateau: A Cretaceous large igneous
680 province in the southwest Pacific Ocean, *Journal of Geophysical Research: Solid Earth*,
681 *101*(B1), 687-696.

682 Navalpakam, R. S., I. A. Pecher, and T. Stern (2012), Weak and segmented bottom simulating
683 reflections on the Hikurangi Margin, New Zealand—Implications for gas hydrate reservoir
684 rocks, *Journal of Petroleum Science and Engineering*, *88*, 29-40.

685 Nicol, A., and J. Beavan (2003), Shortening of an overriding plate and its implications for slip
686 on a subduction thrust, central Hikurangi Margin, New Zealand, *Tectonics*, *22*(6).

687 Nicol, A., and L. M. Wallace (2007), Temporal stability of deformation rates: Comparison of
688 geological and geodetic observations, Hikurangi subduction margin, New Zealand, *Earth and*
689 *Planetary Science Letters*, *258*(3-4), 397-413.

690 Nole, M., H. Daigle, A. E. Cook, A. Malinverno, and P. B. Flemings (2018), Burial-driven
691 methane recycling in marine gas hydrate systems, *Earth and Planetary Science Letters*, *499*,
692 197-204.

693 Papenberg, C. (2004), Seismic investigations of a bottom simulating reflector: implications on
694 gas hydrate and free gas at Southern Hydrate Ridge, 135 pp, Christian Albrechts University,
695 Kiel.

696 Pecher, I. A., S. A. Henrys, and H. Zhu (2004), Seismic images of gas conduits beneath vents
697 and gas hydrates on Ritchie Ridge, Hikurangi Margin, New Zealand, *New Zealand Journal of*
698 *Geology and Geophysics*, *47*(2), 275-279.

699 Pecher, I. A., et al. (2010), Focused fluid expulsion on the Hikurangi Margin, New Zealand –
700 Evidence from possible local upwarping of the base of gas hydrate stability, *Marine Geology*,
701 *272*(1-4), 99-113. doi:110.1016/j.margeo.2009.1010.1006.

702 Plaza-Faverola, A., D. Klaeschen, P. Barnes, I. Pecher, S. Henrys, and J. Mountjoy (2012),
703 Evolution of fluid expulsion and concentrated hydrate zones across the southern Hikurangi
704 subduction margin, New Zealand: An analysis from depth migrated seismic data,
705 *Geochemistry, Geophysics, Geosystems*, *13*(8), Q08018.

706 Plaza-Faverola, A., I. Pecher, G. Crutchley, P. M. Barnes, S. Bünz, T. Golding, D. Klaeschen, C.
707 Papenberg, and J. Bialas (2014), Submarine gas seepage in a mixed contractional and shear
708 deformation regime: Cases from the Hikurangi oblique-subduction margin, *Geochemistry,*
709 *Geophysics, Geosystems*, *15*(2), 416-433.

710 RPS Energy Pty Ltd (2010), Petroleum Report 4158 – Pegasus Basin, Bounty Trough and SAKHE
711 Seismic Acquisition Report*Rep.*, New Zealand Petroleum and Minerals, Wellington.

712 Schwalenberg, K., M. Haeckel, J. Poort, and M. Jegen (2010a), Evaluation of gas hydrate
713 deposits in an active seep area using marine controlled source electromagnetics: Results from
714 Opouawe Bank, Hikurangi Margin, New Zealand, *Marine Geology*, *272*(1-4), 79-88.

715 Schwalenberg, K., W. Wood, I. Pecher, L. Hamdan, S. Henrys, M. Jegen, and R. Coffin (2010b),
716 Preliminary interpretation of electromagnetic, heat flow, seismic, and geochemical data for
717 gas hydrate distribution across the Porangahau Ridge, New Zealand, *Marine Geology*, *272*(1-
718 4), 89-98.

719 Shankar, U., M. Riedel, and A. Sathe (2010), Geothermal modeling of the gas hydrate stability
720 zone along the Krishna Godavari Basin, *Marine Geophysical Researches*, *31*(1-2), 17-28.

721 Shipley, T. H., M. H. Houston, R. T. Buffler, F. J. Shaub, K. J. McMillen, J. W. Ladd, and J. L.
722 Worzel (1979), Seismic reflection evidence for widespread occurrence of possible gas-hydrate
723 horizons on continental slopes and rises, *Am. Assoc. Petroleum Geol. Bull.*, *63*, 2204-2213.

724 Sloan, E. D. (2003), Fundamental principles and applications of natural gas hydrates, *Nature*,
725 *426*(6964), 353-359.

726 Stolt, R. H., and A. K. Benson (1986), *Seismic migration: Theory and practice*, Pergamon.

727 Torres, M., A. M. Trehu, N. Cespedes, M. Kastner, U. Wortmann, J.-H. Kim, P. Long, A.
728 Malinverno, J. Pohlman, and M. Riedel (2008), Methane hydrate formation in turbidite
729 sediments of northern Cascadia, IODP Expedition 311, *Earth and Planetary Science Letters*,
730 *271*(1-4), 170-180.

731 Townend, J. (1997), Estimates of conductive heat flow through bottom-simulating reflectors
732 on the Hikurangi and southwest Fiordland continental margins, New Zealand, *Marine*
733 *Geology*, *141*, 209-220.

734 Tréhu, A. M., D. S. Stakes, C. D. Bartlett, J. Chevallier, R. A. Duncan, S. K. Goffredi, S. M. Potter,
735 and K. A. Salamy (2003), Seismic and seafloor evidence for free gas, gas hydrates, and fluid
736 seeps on the transform margin offshore Cape Mendicino, *Journal of Geophysical Research*,
737 *108*(B5), 2263, doi:2210.1029/2001JB001679.

738 Tréhu, A. M., et al. (2004), Three-dimensional distribution of gas hydrate beneath southern
739 Hydrate Ridge: Constraints fom ODP Leg 204, *Earth and Planetary Science Letters*, *222*, 845-
740 862.

741 Turco, F., G. J. Crutchley, A. R. Gorman, J. J. Mountjoy, J. I. Hillman, and S. Woelz (2020),
742 Seismic velocity and reflectivity analysis of concentrated gas hydrate deposits on the southern
743 Hikurangi Margin (New Zealand), *Marine and Petroleum Geology*, *120*, 104572.

744 Uchida, T., S. Takeya, E. M. Chuvilin, R. Ohmura, J. Nagao, V. S. Yakushev, H. Minagawa, T.
745 Ebinuma, and H. Narita (2004), Decomposition of methane hydrates in sand, sadstone, clays,
746 and glass beads, *Journal of Geophysical Research*, *109*, doi:10.1029/2003JB002771.

747 Vanneste, M., M. De Batist, A. Golmshtok, A. Kremlev, and W. Versteeg (2001), Multi-
748 frequency seismic study of gas hydrate-bearing sediments in Lake Baikal, Siberia, *Marine*
749 *Geology*, *172*(1-2), 1-21.

750 Wood, W. T., and J. F. Gettrust (2001), Deep-tow seismic investigations of methane hydrates,
751 in *Natural gas hydrates: Occurrence, distribution, and detection*, edited by C. K. Paull and W.
752 P. Dillon, pp. 165-178, American Geophysical Union.

753 Wood, W. T., W. S. Holbrook, M. K. Sen, and P. L. Stoffa (2008), Full waveform inversion of
754 reflection seismic data for ocean temperature profiles, *Geophysical Research Letters*, *35*,
755 L04608, doi:04610.01029/02007GL032359.

756 Woodside, W., and J. Messmer (1961), Thermal conductivity of porous media II. Consolidated
757 rocks, *Journal of Applied Physics*, *32*(9), 1699-1706.

758 Yilmaz, Ö. (1987), *Seismic Data Analysis - Processing, Inversion, and Interpretation of Seismic*
759 *Data*, 1000 pp., Society of Exploration Geophysicists, Tulsa.

760 Zwart, G., J. C. Moore, and G. R. Cochrane (1996), Variations in temperature gradients identify
761 active faults in the Oregon accretionary prism, *Earth and Planetary Science Letters*, *139*(3-4),
762 485-495.
763

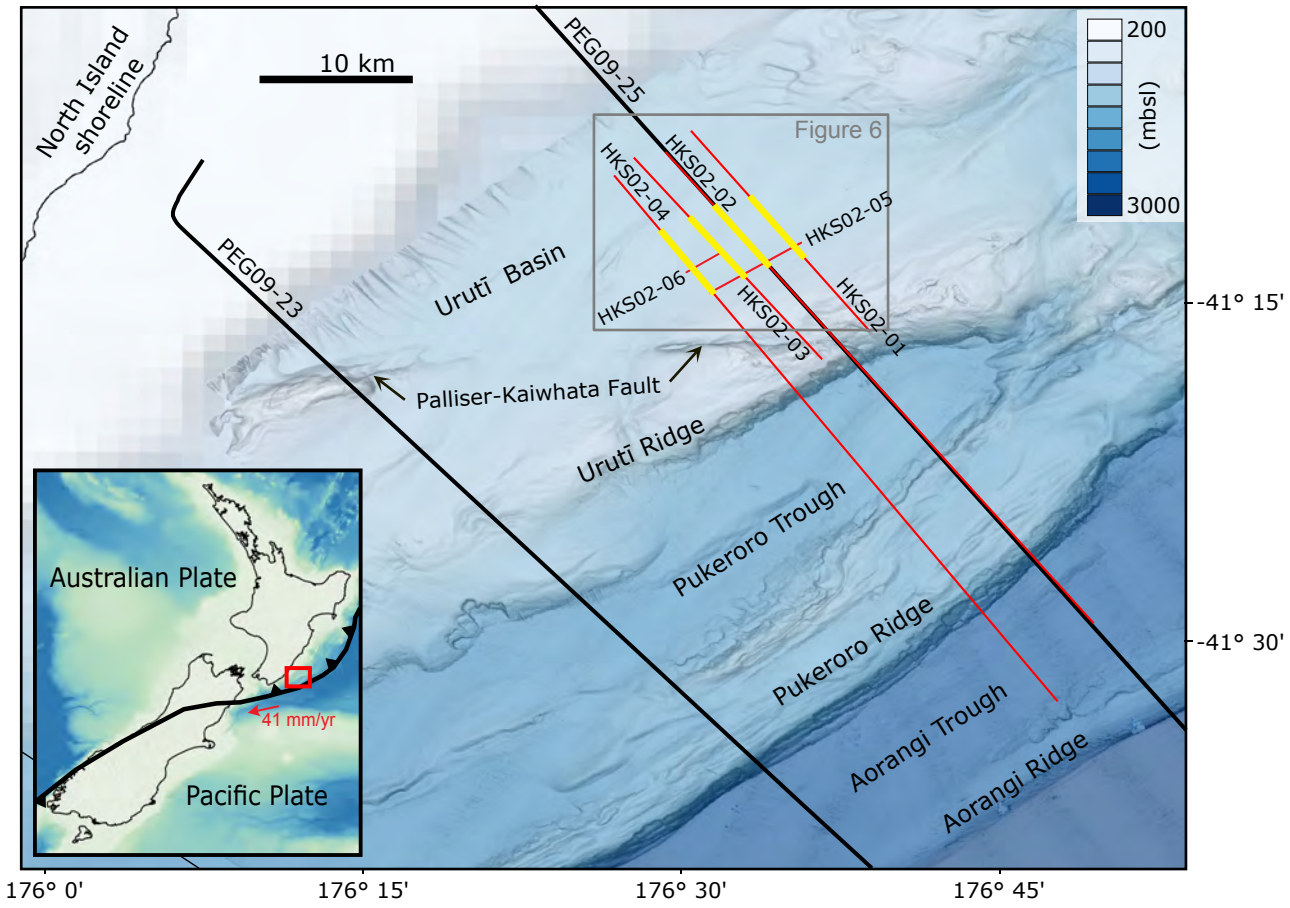
North Island shoreline
10 km
PEG09-25
PEG09-23
Figure 6
HKS02-02
HKS02-04
HKS02-05
HKS02-06
HKS02-03
HKS02-01
200
(mbsl)
3000
Urutī Basin
Palliser-Kaiwhata Fault
Urutī Ridge
Pukeroro Trough
Pukeroro Ridge
Aorangi Trough
Aorangi Ridge
Australian Plate
41 mm/yr
Pacific Plate
-41° 15'
-41° 30'
176° 0'
176° 15'
176° 30'
176° 45'

Figure 1

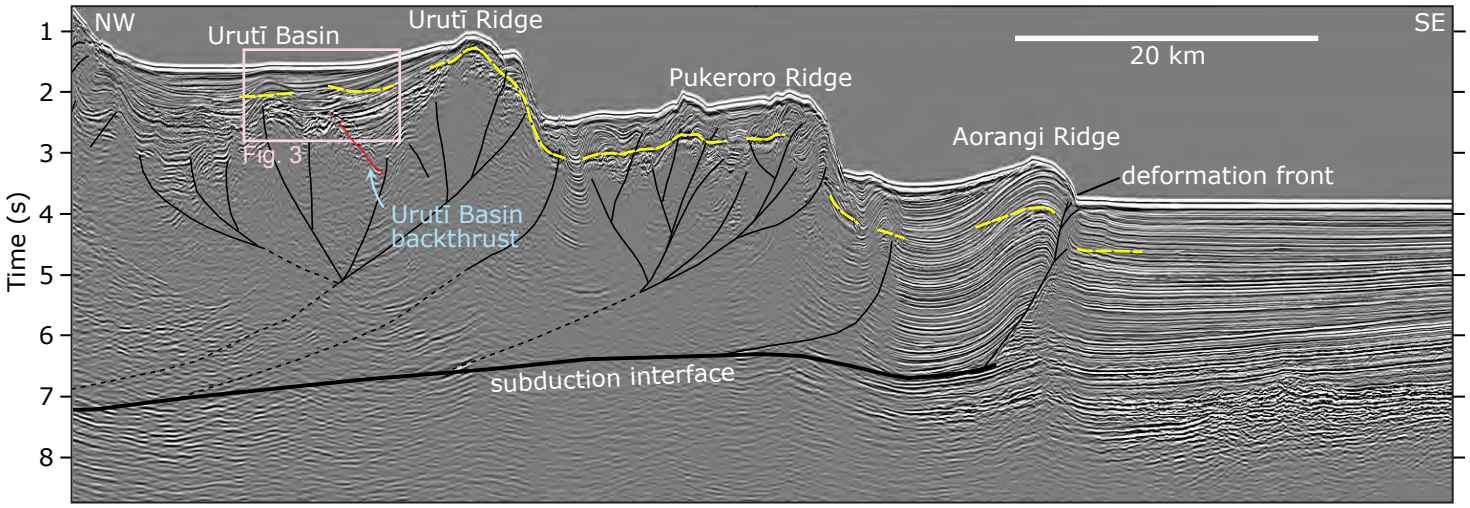
NW
SE
Urutī Basin
Urutī Ridge
Pukeroro Ridge
Aorangi Ridge
20 km
deformation front
Fig. 3
Urutī Basin
backthrust
subduction interface
Time (s)
1
2
3
4
5
6
7
8

Figure 2

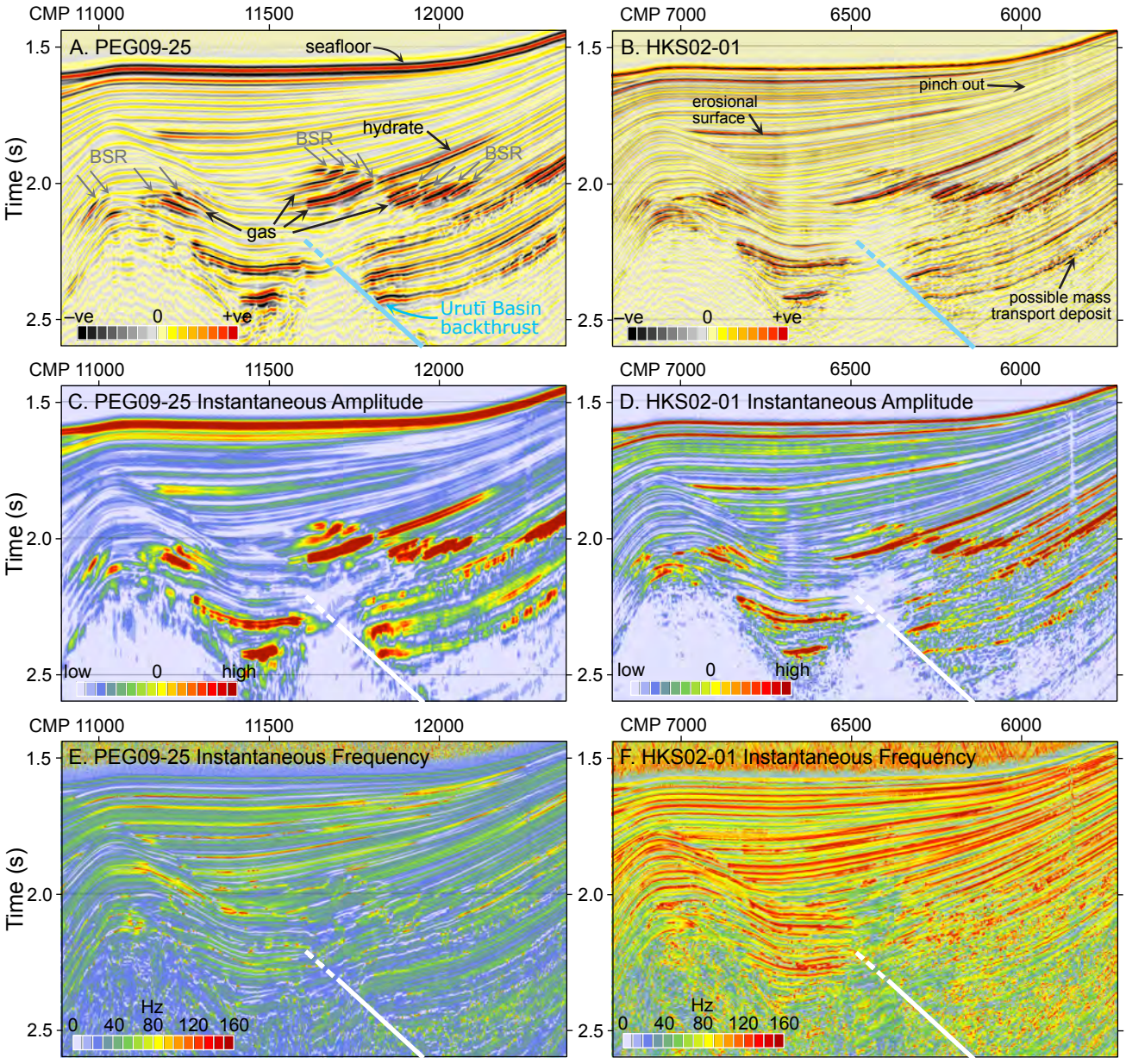
CMP 11000
11500
12000
A. PEG09-25
seafloor
BSR
BSR
BSR
hydrate
gas
Urutí Basin
backthrust
–ve
0
+ve
Time (s)
1.5
2.0
2.5
CMP 7000
6500
6000
B. HKS02-01
pinch out
erosional
surface
possible mass
transport deposit
C. PEG09-25 Instantaneous Amplitude
low
high
D. HKS02-01 Instantaneous Amplitude
E. PEG09-25 Instantaneous Frequency
Hz
0 40 80 120 160
F. HKS02-01 Instantaneous Frequency

Figure 3

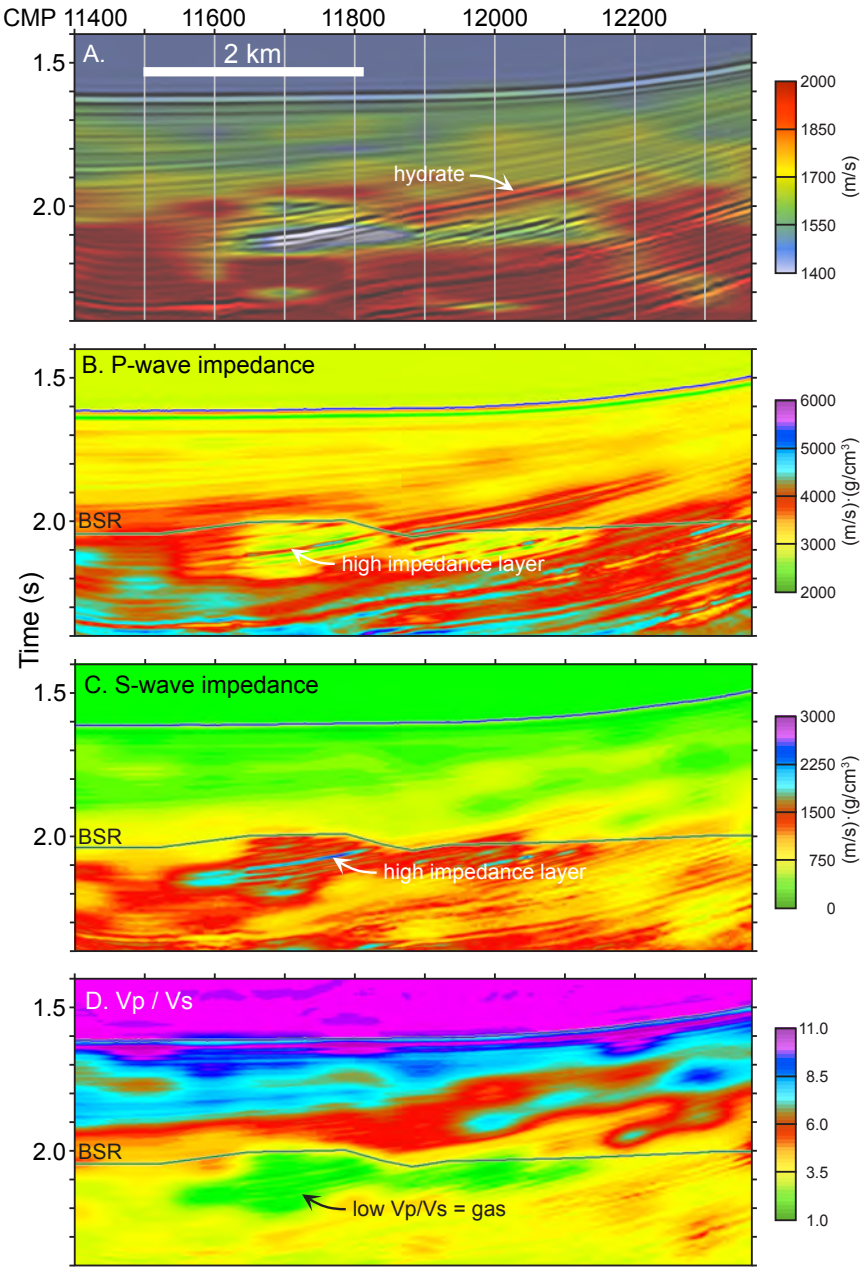
CMP 11400
11600
11800
12000
12200
A.
2 km
hydrate
2000
1850
1700
1550
1400
(m/s)
B. P-wave impedance
BSR
high impedance layer
6000
5000
4000
3000
2000
(m/s)·(g/cm³)
C. S-wave impedance
BSR
high impedance layer
3000
2250
1500
750
0
(m/s)·(g/cm³)
D. Vp / Vs
BSR
low Vp/Vs = gas
11.0
8.5
6.0
3.5
1.0
Time (s)
1.5
2.0

Figure 4

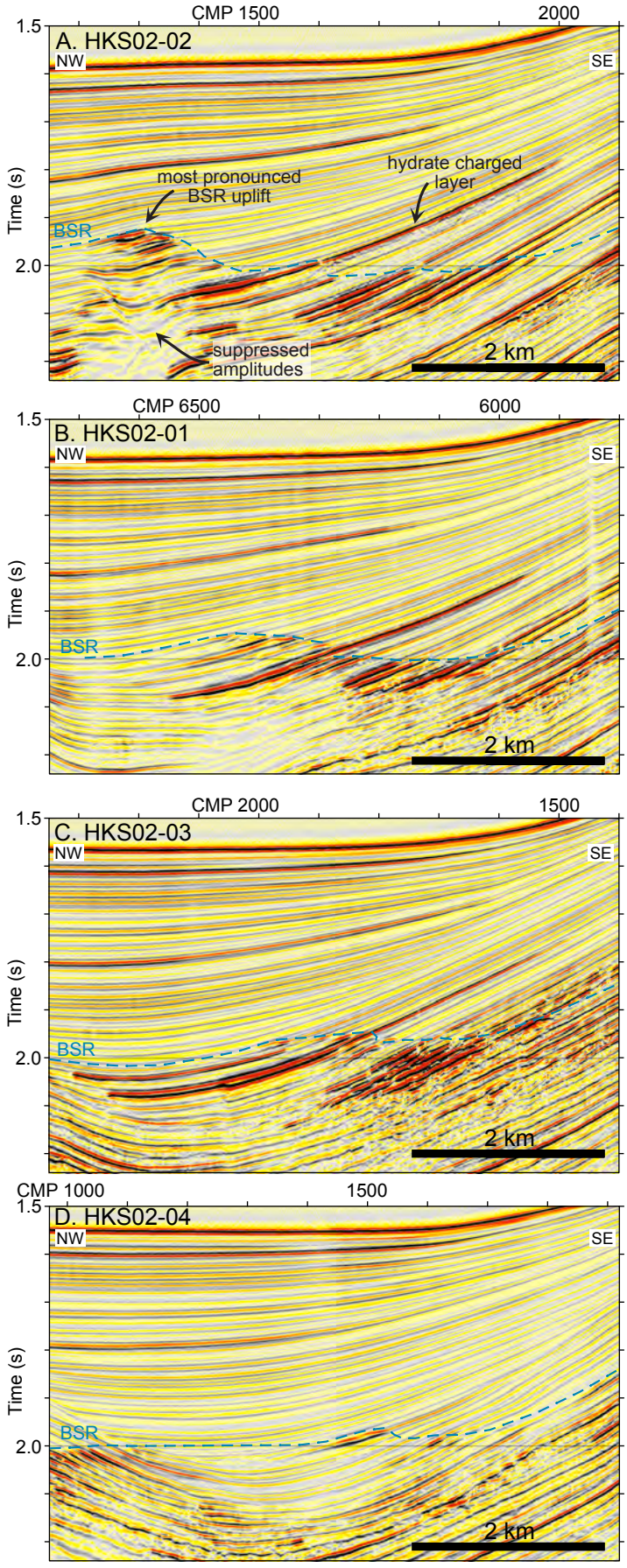
CMP 1500
2000
A. HKS02-02
NW
SE
most pronounced
BSR uplift
hydrate charged
layer
BSR
suppressed
amplitudes
2 km
Time (s)
1.5
2.0
CMP 6500
6000
B. HKS02-01
NW
SE
BSR
2 km
Time (s)
CMP 2000
1500
C. HKS02-03
NW
SE
BSR
2 km
Time (s)
CMP 1000
1500
D. HKS02-04
NW
SE
BSR
2 km
Time (s)

Figure 5

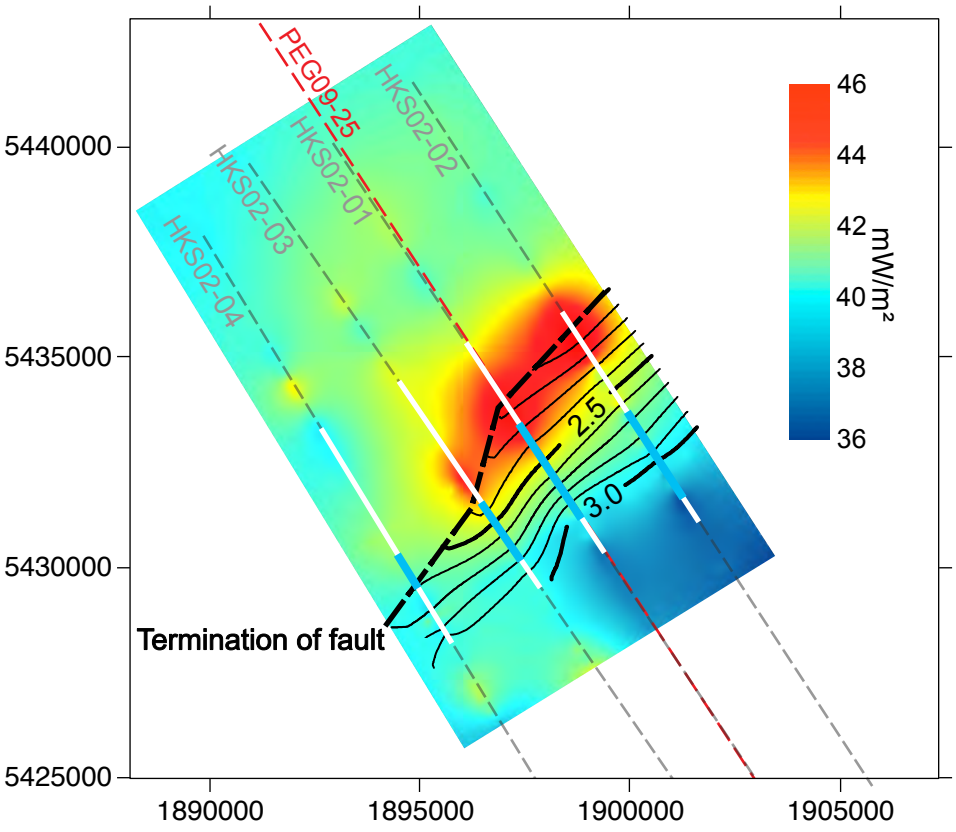
PEG09-25
HKS02-01
HKS02-02
HKS02-03
HKS02-04
46
44
42
40
38
36
mW/m²
2.5
3.0
Termination of fault
5440000
5435000
5430000
5425000
1890000
1895000
1900000
1905000

Figure 6

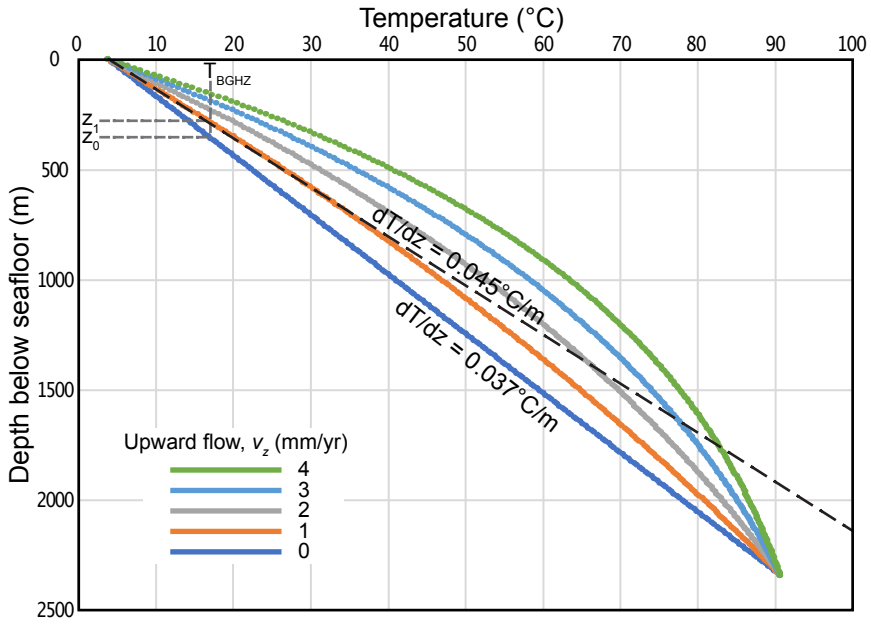
Temperature (°C)
0
10
20
30
40
50
60
70
80
90
100
Depth below seafloor (m)
0
500
1000
1500
2000
2500
T BGHZ
Z
Z0
1
dT/dz = 0.045°C/m
dT/dz = 0.037°C/m
Upward flow, vz (mm/yr)
4
3
2
1
0

Figure 7

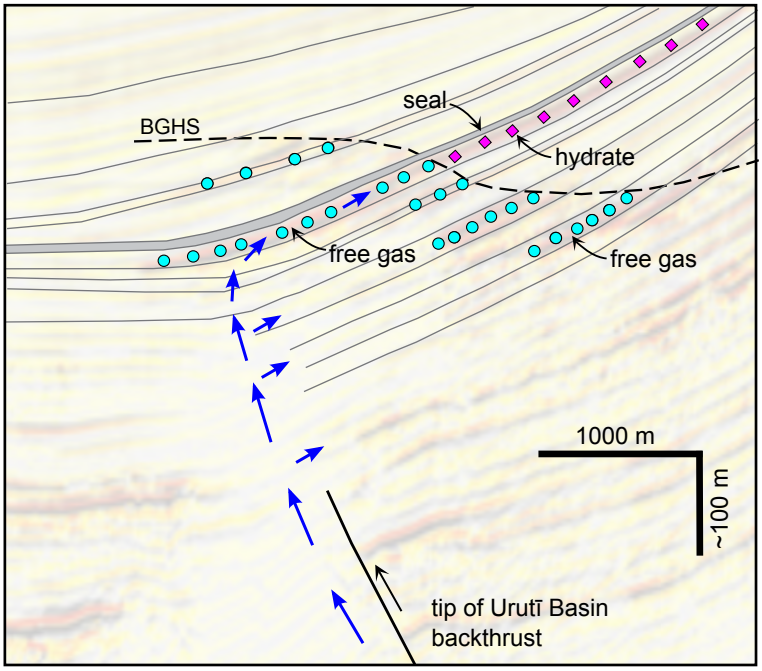
seal
BGHS
hydrate
free gas
free gas
1000 m
~100 m
tip of Urutī Basin
backthrust

Figure 8